

Article

Analysis of Scattering Properties of Continuous Slow-Release Slicks on the Sea Surface Based on Polarimetric Synthetic Aperture Radar

Guannan Li ^{1,2}, Ying Li ^{1,2,*}, Bingxin Liu ^{1,2} , Yongchao Hou ^{1,2} and Jianchao Fan ³

¹ Navigation College, Dalian Maritime University, Dalian 116026, China; lgn@dlmu.edu.cn (G.L.); gisbingxin@dlmu.edu.cn (B.L.); houyongchao@dlmu.edu.cn (Y.H.)

² Environmental Information Institute, Dalian Maritime University, Dalian 116026, China

³ National Marine Environmental Monitoring Center, Dalian 116026, China; fjchaonmemc@163.com

* Correspondence: yldmu@dlmu.edu.cn; Tel.: +86-411-8472-6829

Received: 20 May 2018; Accepted: 18 June 2018; Published: 21 June 2018



Abstract: This study employs polarimetric synthetic aperture radar (Pol-SAR) to examine the scattering properties of continuous slow-release oil slicks on the sea surface. The objective is to extract and analyze the general polarization scattering properties of continuous slow-release slicks, i.e., those slicks that consist of substances released at a fairly slow and relatively constant rate, and to determine the influence of the slick formation process on these properties. Using multi-polarization feature parameters derived from the averaged coherency matrix, we find that the scattering mechanisms related to the continuous slow-release slicks differ from those of anthropogenic slicks, possibly as a result of the multiple scattering mechanisms that occur between the interfaces formed by the thick slick layer. Combinations of entropy (H) and modified anisotropy (A_{12}) are relatively robust parameters for identifying continuous slow-release slicks under different sea conditions, and may serve as a reference parameter for slick detection.

Keywords: SAR; continuous slow-release slick; polarimetric scattering feature; oil spill

1. Introduction

Oil spills, whether in open water or near shorelines, are considered a serious environmental pollution problem. Oil pollution has received extensive public attention on account of the resulting ecological destruction, including oil floating on the sea surface, residual oil deposited on coastlines, sunken and submerged oil, oiled marine animals, and areas of oil-polluted sea ice [1–4]. Alves and Zodiatis have conducted some of the most complete studies of oil spill response in the form of an assessment of the impact of oil spills on human activity and shorelines; offshore susceptibility; and clean-up, and mitigation efforts in the Mediterranean Basin and the Baltic Sea based on some worthy projects on oil spill response [5–8]. There are two main mechanisms by which marine slicks form on the sea surface. The first mechanism includes oil spills caused by human activities such as ship accidents, local spills near harbors, utilization, and discharge, which are usually considered to be relatively direct and rapid-release slicks on the sea surface within a certain time limit. The second involves oil seepage at a fairly slow and relatively constant rate, giving rise to what can be termed as continuous slow-release slicks, such as natural oil seeps and biogenic slicks [9,10]. Natural oil seeps are the single most significant source, accounting for approximately 47% of the total petroleum compounds released each year [9,11,12]. Being frequently less visible, natural oil seeps often receive less consideration than oil spills from maritime accidents. Biogenic slicks consist of surface-active organic compounds that are composed of a hydrophobic part and a hydrophilic part, and are released by marine plants

and microorganisms. This special amphiphilic structure leads to the spontaneous distribution of surface active substances at the air-sea interface to form monomolecular slicks [13]. These slicks exhibit surface roughness-damping capabilities similar to those of oil spills, which can increase the ambiguity of oil spill identification and tracking. In order to deal with oil spill emergencies, post-disaster pollution control, and the development and assessment of marine resources, it is important to acquire instantaneous information on the location, magnitude, type, and scattering characteristics of the slick [5–8]. Consequently, authorities worldwide have made significant efforts to develop remote sensing technologies that can provide extensive coverage, continuous observation, rich data that are required to detect and monitor oil on the ocean surface. From the perspective of post-disaster planning and oil spill tracking, research on the scattering properties of continuous slow-release slicks can assist in assessing the causes and sources of slicks and reduce the errors inherent in tracking oil spills. From the perspective of environmental monitoring and assessment, it can provide more comprehensive information for the assessment of the marine ecological environment. For example, natural oil seeps can be considered as a reference for reducing the ambiguity of oil slick recognition. Moreover, biogenic slicks reflect indirectly the changes occurring in the surrounding marine ecosystem. From the perspective of economic development, the analysis and identification of continuous slow-release slicks can assist in the search for new economic development projects; for example, natural oil seeps can provide information for exploring petroleum systems, while biogenic slicks can provide information for evaluating the stability and biodiversity of a marine environment, and can provide information for exploring new fisheries [14]. Thus, in addition to differentiating slick types by interpreting their shape and size information from satellite synoptic views; it is valuable to explore more comprehensive information pertaining to continuous slow-release slicks. To date, numerous studies have reported the use of optical remote sensing, even though the application of optical sensors is typically limited by cloud cover, poor weather, and lack of contrast [1,15].

Pol-SAR (Polarimetric Synthetic Aperture Radar) is widely applied to marine environmental monitoring, target recognition, and land-cover classification. In contrast to passive optical sensors, Pol-SAR systems utilize their own active illumination systems and offer the potential for large-area observation during day and night, and near all-weather remote sensing [16–18]. In addition, Pol-SAR systems transmit and receive electromagnetic pulses in both horizontal and vertical polarizations, which can obtain sufficient amplitude and phase information on each resolved image pixel [19]. The scattering properties and the dominant scattering mechanism of various marine slicks can be extracted and interpreted by exploiting comprehensive polarization information. Pol-SAR has been used widely in the detection and mapping of oil spills even under conditions of wind and rain [1,20–22]. In recent years, a growing number of studies on oil spill detection, simulation of oil spill behavior, and the interpretation of polarization scattering characteristics have shown promising results. Alves et al. have published various models of oil spill behavior [5–8,23,24]. Stine et al. compared and analyzed multi-polarization features of SAR data using an artificial oil spill exercise at the Frigg field situated northwest of Stavanger [25]. Ferdinando et al. proposed a polarimetric model related to the degree of polarization to distinguish natural oil seeps and look-alikes using quad-polarization SAR data [26]. Salberg et al. and Li et al. proposed and reviewed several strategies for oil spill detection using hybrid-polarimetric SAR data [27,28]. Those studies [29–34] also proposed some valuable methods and demonstrated the potential and utility of Pol-SAR-based oil spill detection, but they focused on the extraction of oil spills rather than characterizing the polarization scattering associated with continuous slow-release slicks. In contrast, several studies have made use of surface-active substances (such as peanut oil, oleyl alcohol, oleic acid methyl ester, and methyl palmitate) that form monomolecular slicks to simulate biogenic slicks for analyzing and exploring the damping behavior and their potential influence on remote sensing signals [13,30,35,36]. Despite some further studies with different SAR sensors on the scattering properties of natural oil seeps and biogenic slicks [13,14,19,35,37,38], comprehensive analysis of and research into continuous slow-release slicks remains deficient.

Comparisons between continuous slow-release oils and anthropogenic sea surface slicks are scarce, especially those that capture images at the same time, in the same research area, utilizing the same airborne/spaceborne sensors [13]. Herein, the situation described above and a brief inspiration from other published work forms the background to the present study [13,30,35–37], which contains two main research objectives. The first is to extract the general polarization scattering properties of continuous slow-release slicks through qualitative and quantitative analysis of two typical continuous slow-release slicks (natural oil seeps and biogenic slicks) and investigate the underlying scattering mechanisms using the same Pol-SAR system. The second is to explore how the formation process of marine slicks influences the resulting scattering properties, through quantitative analysis of the differences between biogenic slick (as the continuous slow-release monomolecular slick) and peanut oil (as the anthropogenic sea surface monomolecular slick simulating biogenic slicks [13,30,35]) in the same location being monitored by the same sensors.

2. Experimental Design and Methodology

2.1. Experimental Design

Continuous slow-release slicks comprise substances released at a fairly slow and relatively constant rate [9,10]. In this study, two typical continuous slow-release slicks based on quad-polarization RADARSAT-2 data are used for two research cases: natural oil seeps and biogenic slicks. The formation process for two typical continuous slow-release slicks is shown in Figure 1. RADARSAT-2 provides multi-polarization and multi-beam operation modes, including Spotlight, Fine, Wide, Standard, and ScanSAR, in linear single-, dual- and quad-modes. The capabilities of RADARSAT-2 full polarization, incorporating an extremely low noise-floor and cross-talk correction of different channels, make it a remarkable system for the basis of subsequent research [19,37]. The SAR data in this paper are further characterized in Table 1.

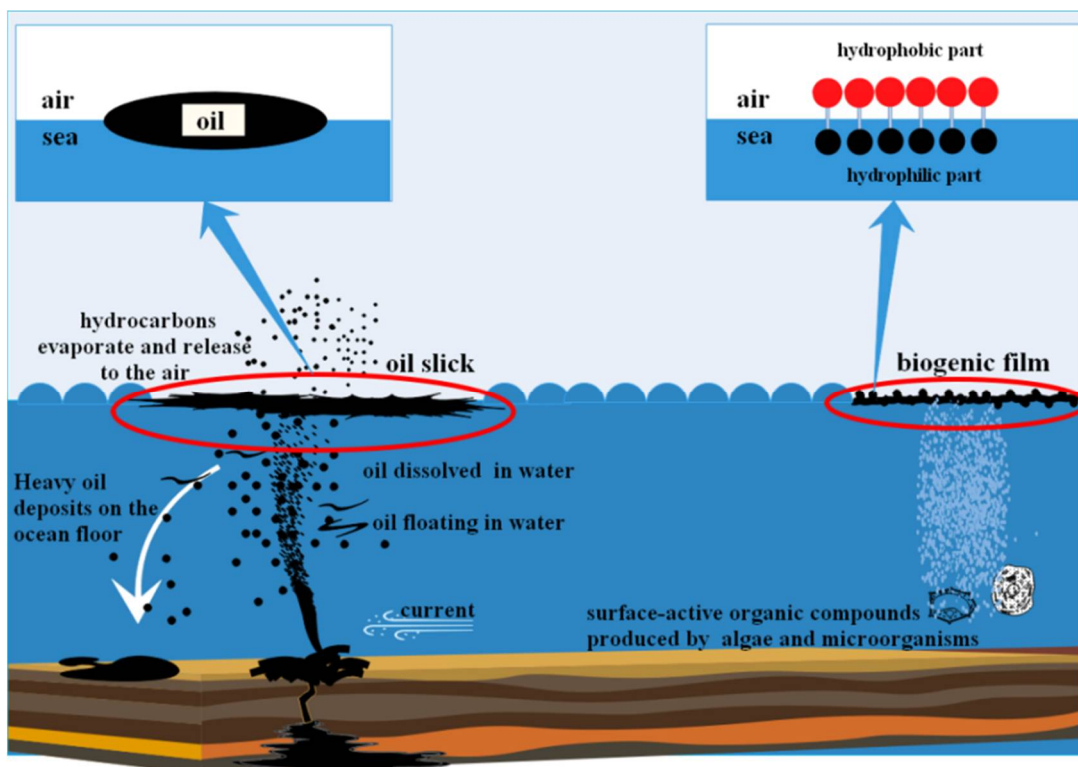


Figure 1. Schematic of natural oil seeps and biogenic slicks formed in the ocean environment.

Table 1. Parameter properties of SAR data in two Cases.

Case/Sensor	Case 1 (RADARSAT-2)	Case 2 (RADARSAT-2)
Date	8 May 2010	18 September 2009
Time	12:01 a.m. (UTC)	10:49 a.m. (UTC)
Region	The Gulf of Mexico (26°48' N, 92°02' W)	The South China Sea (18°06' N, 109°24' E)
Mode/Product	Fine Quad-Pol mode SLC	Fine Quad-Pol mode SLC
Frequency	C-band (5.405 GHz)	C-band (5.405 GHz)
Incidence angle	41.9–43.4°	32.3–34.1°
Resolution ($R_g \times A_z$)	5.2 × 7.6 (m)	5.2 × 7.6 (m)
Pixel space ($R_g \times A_z$)	4.7 × 5.1 (m)	4.7 × 5.1 (m)
Polarization	HH, HV, VH, VV	HH, HV, VH, VV
Wind speed/wind direction	6.5 m/s (167°)	10 m/s

2.2. Dataset

The RADARSAT-2 image in Case 1 was acquired over the Gulf of Mexico on 8 May 2010 and covers a well-known oil spill region. The incidence angles range from 41.9° (near range) to 43.4° (far range); and visible dark spots have been interpreted as natural crude oil seeps (as the continuous slow-release slick), as these are common at this location (Figure 2) [39].

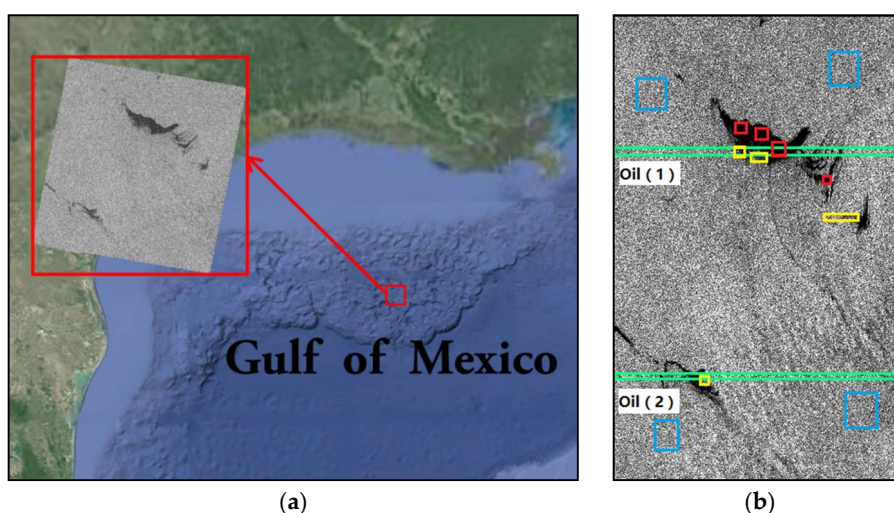


Figure 2. Natural oil seeps scene of RADARSAT-2 (8 May 2010): (a) Location of the acquired image; (b) Intensity images (σ_{VV}). The colored boxes indicate sample regions used in noise equivalent sigma zero (NESZ) analysis (blue: sea, red: thick oil region, yellow: thin oil region). The green rectangles in (b) denote areas that include thick oil areas, thin oil areas, and clean-ocean surface areas.

The RADARSAT-2 image in Case 2 was acquired over the South China Sea, and shows a simulated natural biogenic slick. Approximately 5 L of peanut oil were deliberately poured onto the sea surface in order to simulate a biogenic slick and the atmospheric front in the vicinity of the slick. The data have been studied in other papers [30,35]. The incidence angles ranged from 32.4° to 34.1° (Figure 3). The experiment location is near a popular fishing region off the coast of China's Hainan Island [35]. It should be noted that biogenic slicks and peanut oil slicks are both considered to be the same type of monomolecular slick; thus, research into the scattering properties of the monomolecular slick produced by five liters of peanut oil can be used as a reference for future research.

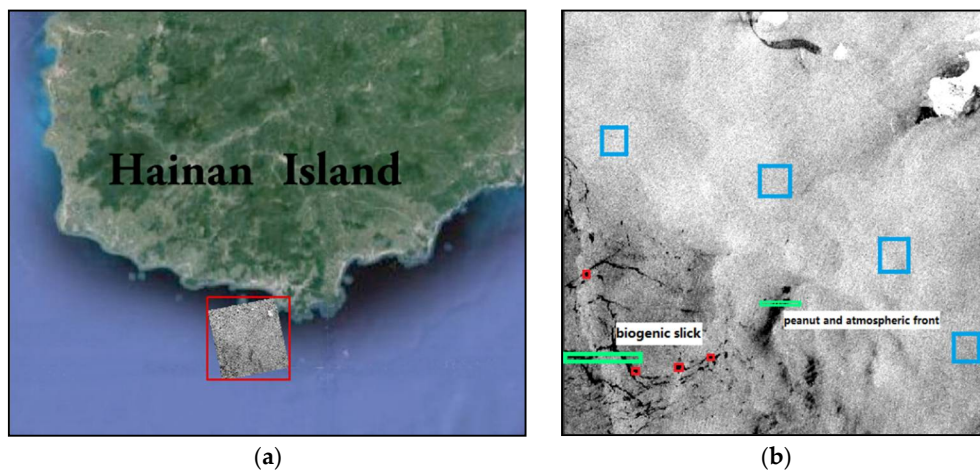


Figure 3. The scene of RADARSAT-2 acquisition (18 September 2009), showing natural and simulated (peanut oil) biogenic slicks: (a) Location of the acquired image; (b) Intensity images (σ_{VV}).

2.3. Noise Analysis

Radar backscatter signals from the target, such as oil spills, biogenic slicks, and look-alikes, return only part of the total incident radar power [18]. The noise equivalent sigma zero (NESZ) is the noise-floor in the SAR operating system, which represents the radar backscatter cross-section of the signal level, equivalent to that from the noise of the instrument. The magnitude of NESZ is influenced by the radar antenna power, antenna gain, system power consumption, and system ambient temperature. The normalized radar cross section (NRCS) data that are lower than the NESZ are regarded as corrupted by noise. Hence, NESZ, the benchmark for measuring the detection limit of the backscatter signal, is useful and important for analyzing the signal level of the targets.

Noise analyses are implemented based on the two RADARSAT-2 data series in Section 3. The NRCS of each polarization channel is plotted with the NESZ to analyze the signal level. The backscatter values σ_0 in the sampling areas, labeled as blue/red/yellow/green boxes in Figures 2 and 3, represent the distribution of the sample data.

2.4. Methodology

Radar polarization information can be used to study the surface characteristics of continuous slow-release oil slicks. Interpretation and analysis of polarization information can capture important indicators of scattered signals, derived from the slick surfaces. Some prior studies have demonstrated the ability of polarization decomposition methods to analyze and evaluate the scattering properties of marine slicks [18,25,29,40]. In this paper, the parametric analysis of RADARSAT-2 data is primarily grounded in the eigenvalue- and eigenvector-based Cloude polarization decomposition algorithm, including H/α calculated by [41], anisotropy A_{12} revised by [25], and volume scattering index (VSI) introduced by [42,43].

A fully polarimetric SAR scattering matrix S is given as:

$$S = \begin{bmatrix} S_{HH} & S_{VH} \\ S_{HV} & S_{VV} \end{bmatrix} \quad (1)$$

Here, matrix elements S_{xy} , with $x, y \in \{H, V\}$, where x represents transmit, y represents receive, and H and V represent horizontal and vertical polarizations, respectively. The coherence matrices T can be constructed based on the Pauli scattering vector k , which can be obtained from the scattering matrix S . For a reciprocal medium, the dimension of vector k is 3 and the relation $S_{HV} = S_{VH}$ is satisfied in this paper. The vector k and matrix T are given by [44]:

$$k = \frac{1}{\sqrt{2}} \begin{bmatrix} S_{HH} + S_{VV} & S_{HH} - S_{VV} & 2S_{HV} \end{bmatrix} T \quad (2)$$

$$T = kk^H \quad (3)$$

$$T_3 = \langle k \cdot k^* T \rangle = \begin{bmatrix} T_{11} & T_{12} & T_{13} \\ T_{21} & T_{22} & T_{23} \\ T_{31} & T_{32} & T_{33} \end{bmatrix} \quad (4)$$

$$= \frac{1}{2} \begin{bmatrix} \langle |S_{HH} + S_{VV}|^2 \rangle & \langle (S_{HH} + S_{VV})(S_{HH} - S_{VV})^* \rangle & 2\langle (S_{HH} + S_{VV})S_{HV}^* \rangle \\ \langle (S_{HH} - S_{VV})(S_{HH} + S_{VV})^* \rangle & \langle |S_{HH} - S_{VV}|^2 \rangle & 2\langle (S_{HH} - S_{VV})S_{HV}^* \rangle \\ 2\langle S_{HV}(S_{HH} + S_{VV})^* \rangle & 2\langle S_{HV}(S_{HH} - S_{VV})^* \rangle & 4\langle |S_{HV}|^2 \rangle \end{bmatrix}.$$

Polarimetric features can be obtained using T matrices. Eigenvalues or eigenvectors can be obtained by T matrix decomposition. The eigenvalues λ_i and eigenvectors u_i are given by [45]:

$$T_3 = U_3 \Sigma U_3^{-1} = \sum_{i=1}^{i=3} \lambda_i T_{3i} = \sum_{i=1}^{i=3} \lambda_i u_i u_i^{T*} \quad (5)$$

Entropy is one component of the $H/A_{12}/\alpha$ decomposition that is defined by a logarithmic form of eigenvalues λ_i decomposed with T , among them $\lambda_1 > \lambda_2 > \lambda_3$. Entropy, H , represents the degree of randomness of the scattering mechanisms that dominate the target region, and is given by [45]:

$$H = \sum_{i=1}^3 -P_i \log_3 P_i \quad (6)$$

$$P_i = \frac{\lambda_i}{\sum_{i=1}^3 \lambda_i} \quad (7)$$

The mean scattering angle α is used to describe the underlying scattering mechanism, which usually combines with polarization entropy H and anisotropy A . The mean scattering angle is given by [45]:

$$\alpha = \sum_{i=1}^3 P_i \alpha_i = P_1 \alpha_1 + P_2 \alpha_2 + P_3 \alpha_3 \quad (8)$$

The modified anisotropy A_{12} is calculated based on the two largest eigenvalues of T , and is different from the conventional A , which is calculated using the two smallest eigenvalues [25]. The conventional A can be considered as the effective parameter for measuring small-scale roughness on the sea surface.

$$A_{12} = \frac{\lambda_1 - \lambda_2}{\lambda_1 + \lambda_2} \quad (9)$$

The parameter combination of H and A_{12} , which increase the likelihood of distinguishing different ocean slicks, is proposed to analyze the character of targets, i.e., $(1 - H)^*(1 - A_{12})$, $H^*(1 - A_{12})$, $(1 - H)^* A_{12}$, $H^* A_{12}$.

VSI is a measure of the depolarization of the linearly polarized incident radar signal. The depolarization mechanisms are of the multipath-scattering type. As an indirect measure of multipath scattering elements, VSI is commonly applied to forest and wetland ecosystems. The marine system is highly complex, and the scattering mechanisms of marine films vary according to film thickness, wind speed, wave height, and other factors. The VSI is given as follows (where VV , HH , VH and HV represent the backscatter parameters derived from the matrix elements S_{xy} , respectively) [42,43]:

$$VSI = \frac{VH + HV}{VV + HH + VH + HV} \quad (10)$$

3. Results

3.1. NESZ Analysis

In this section, the NRCS of each polarization channel is plotted to analyze the signal level relative to the NESZ in Figure 4. The box-plots show the minimum, maximum, upper quartile, median, lower quartile, and outliers of the backscatter values σ_0 in sample areas labeled as blue/red/yellow boxes in Figures 2 and 3, which represent the distribution of the sample data. The median is the value separating an ordered data array into two equal parts; the upper quartile is defined as the middle number between the minimum and median of the ordered array sample data, and the lower quartile is the middle number between the maximum and the median.

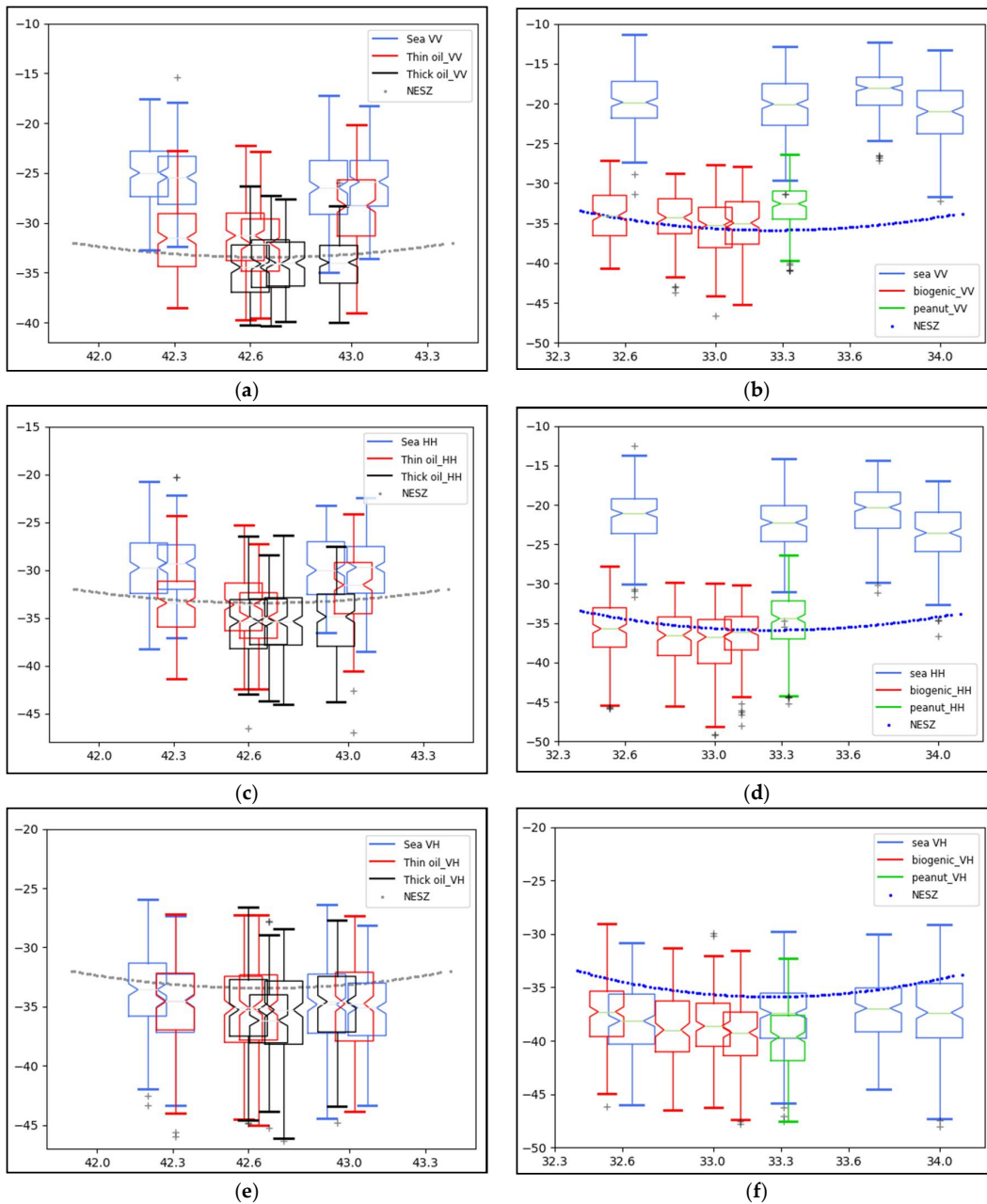


Figure 4. Signal-to-noise analyses: (a) VV channel (Case 1); (b) VV channel (Case 2); (c) HH channel (Case 1); (d) HH channel (Case 2); (e) VH channel (Case 1); (f) VH channel (Case 2). Each box represents the backscatter signal range in the regions indicated by the colored boxes in Figures 2 and 3.

For the imagery in Case 1, three groups of sample data were extracted for follow-up analysis, including seawater, thick oil, and the thin oil slick mixed with water at the boundary of the oil slick. For the VV channel, the signal values of seawater are mostly greater than the NESZ, with the exception of some data at large incident angles. In the thick oil region, the data from both sample areas span the NESZ, with more than 50% of the data being lower than the NESZ values. The data range extends from 7.4 dB below to 6.6 dB above the NESZ baseline, and the data are distributed mostly within the area with a lower backscattering value than that of the sea. In the thin oil area, approximately 50–70% of the data lie above the NESZ baseline. The mixture of oil and water is sufficient at the boundary of the oil spill area, especially in the sample area with high incidence angle. The data values range from 12 dB below to 6.1 dB above the NESZ in the VV. Backscatter decreases faster in the HH channel than in the VV channel, so all the sample data in the HH channel are approximately 5 dB lower than those in the VV channel and thus closer to the noise floor (Figure 4c). As shown in Figure 4e, high noise contamination was observed in returns from all three surfaces in the cross-polarization (VH) channels.

For the imagery in Case 2, the overall values of the sea area are 1.9–7.2 above the NESZ baseline in the VV channel (Figure 4b). In the biogenic slick region, all the data values span the NESZ. Approximately 50–75% of the slick data are higher than the NESZ baseline, and most slick data are distributed in the area with a lower backscattering value than that of the sea. In the area with the peanut oil slick, more than 75% of the data are 2.4 dB above the NESZ baseline; the statistical values of peanut oil slick are much lower than those of the sea and are slightly higher than those of the biogenic slick. On the other hand, the mean HH values lie about 1.3–5.2 dB below the mean VV signal in all the samples (Figure 4d). In the VH channel, all data are contaminated by instrument noise, and fluctuate around the NESZ baseline (Figure 4f).

Analysis of the two images shows that co-polarization channels (VV/HH) have higher signal-to-noise ratios (SNRs) than the cross-polarization (VH/HV) channels, and the backscatter in the VV polarization channel is lower than that in the HH channel. In addition, the noise floor baseline is higher in Case 1 than in Case 2, which results in the image in Case 1 having a higher SNR.

3.2. Polarization Parameters of Continuous Slow-Release Slick

Figure 5 presents the results for entropy analysis in the two cases. The polarization scattering entropy describes the randomness of various scattering types, which are roll-invariant. As shown in Figure 5a,b, seawater is dominated primarily by a single scattering target return from surface Bragg scatter, whose entropy value is lower than those of both crude oil and biogenic slicks. Natural oil seeps and biogenic slicks are clearly distinguished from the ambient ocean with significantly higher H, which indicates that the scattering has relatively strong randomness, and the number of identifiable scattering mechanisms is reduced. For Case 1, the data results extracted from the oil sample area (the green boxes in Figure 2) are shown in Figure 5c,d. The entropy value within the thick oil region increases significantly, with all values being greater than 0.9. The oil slick has multiple scattering mechanisms, including both Bragg and non-Bragg scattering, and thus presents complex characteristics [31]. The entropy values within the thin oil region in Case 1 range from 0.8 to 0.9.

The results show the differences in entropy between the slick (0.6–0.95), ambient sea (0.2–0.4), peanut oil (0.75–0.85), and atmospheric front (0.5–0.7) areas in Case 2. The NESZ baseline is lower in the image with a smaller incidence angle (Case 2) than that with larger incidence angle (Case 1), and signals are less contaminated by noise. Hence, the ambient signal level within the image with small incidence angle (Case 2) has a higher SNR. These results may explain why the ocean has higher entropy in images of natural oil seeps (i.e., with larger incidence angle) than that in images of biogenic slicks (i.e., with smaller incidence angle). These findings concur with those reported in the literature [25].

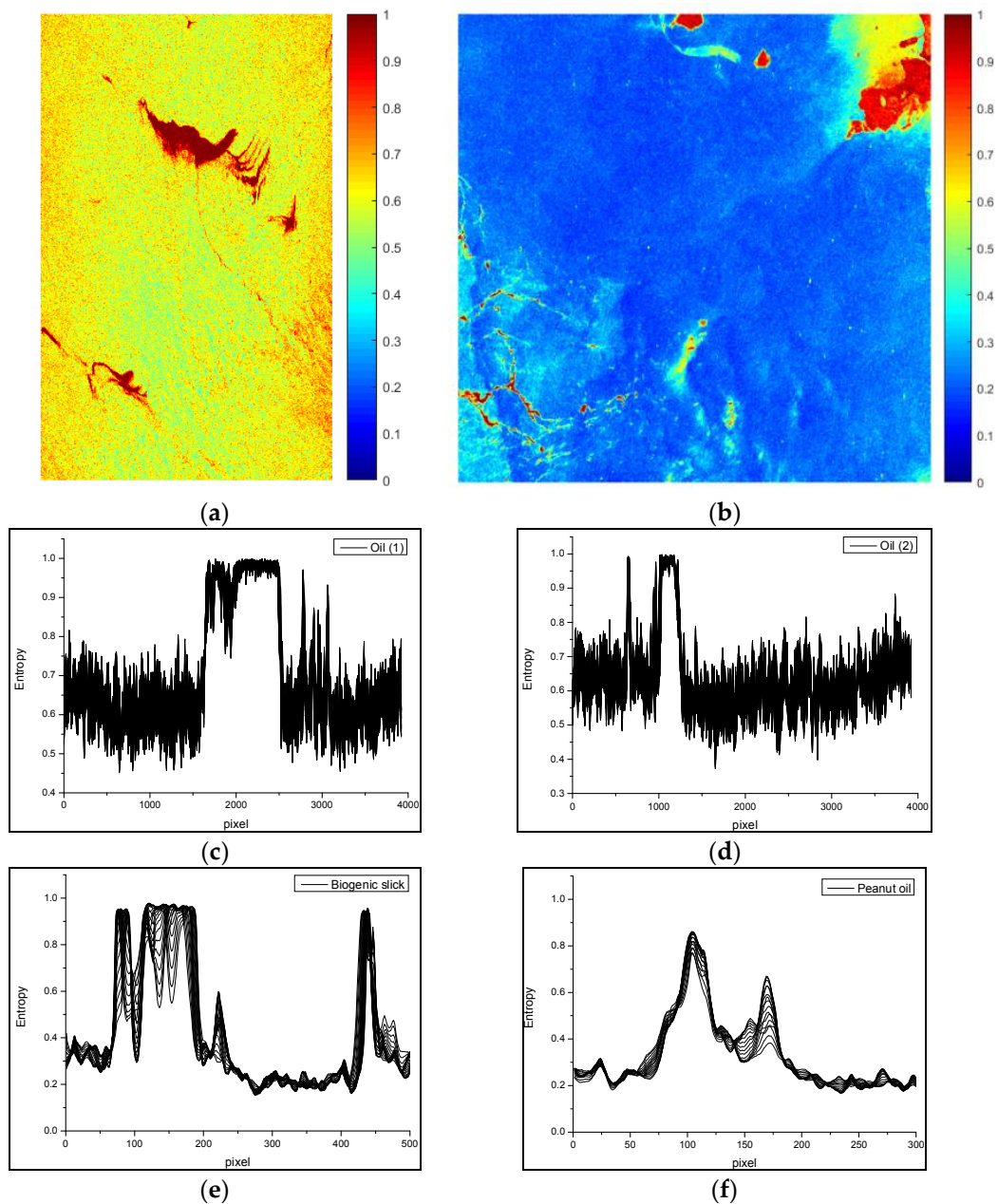


Figure 5. Entropy (H) values from RADARSAT-2 images of the natural oil seep (a) and the biogenic and peanut oil slicks (b); (c–f) the H values for the four green rectangular areas (oil (1), oil (2), biogenic slick, and peanut oil, respectively) that are indicated on the SAR images in Figures 2 and 3.

Figure 6 depicts the character of the mean scattering angle α , which corresponds to the scattering mechanism of the target area. The effective range of α corresponds to the continuous variation of the scattering mechanism. The primary scattering mechanism is surface scatter, including geometrical optics surface scattering, physical optics surface scattering, specular scattering, and Bragg surface scattering when α is $<42.5^\circ$. Dipole scattering is dominant when α is in the range from 42.5° to 47.5° , and double-bounce scattering or even-bounce scattering is dominant when α is in the range 47.5° – 90° . In the ocean area, surface single scattering is the main scattering mechanism. For Case 1, the mean scattering angle α is low ($\sim 30^\circ$) for clean sea areas, indicating that single-bounce surface scatter is dominant. The range of α is around 55 – 65° within the thick oil area, and 45 – 55° within thin oil area, as the presence of oil modifies the scattering mechanism. In addition, the regular ripples caused by

wind, waves, and currents on the sea surface also show similar characteristics to the thin oil slick for α . On the other hand, the α value of seawater is $<15^\circ$, within the range $45\text{--}55^\circ$ for the biogenic slick, and $35\text{--}42^\circ$ for peanut oil in Case 2.

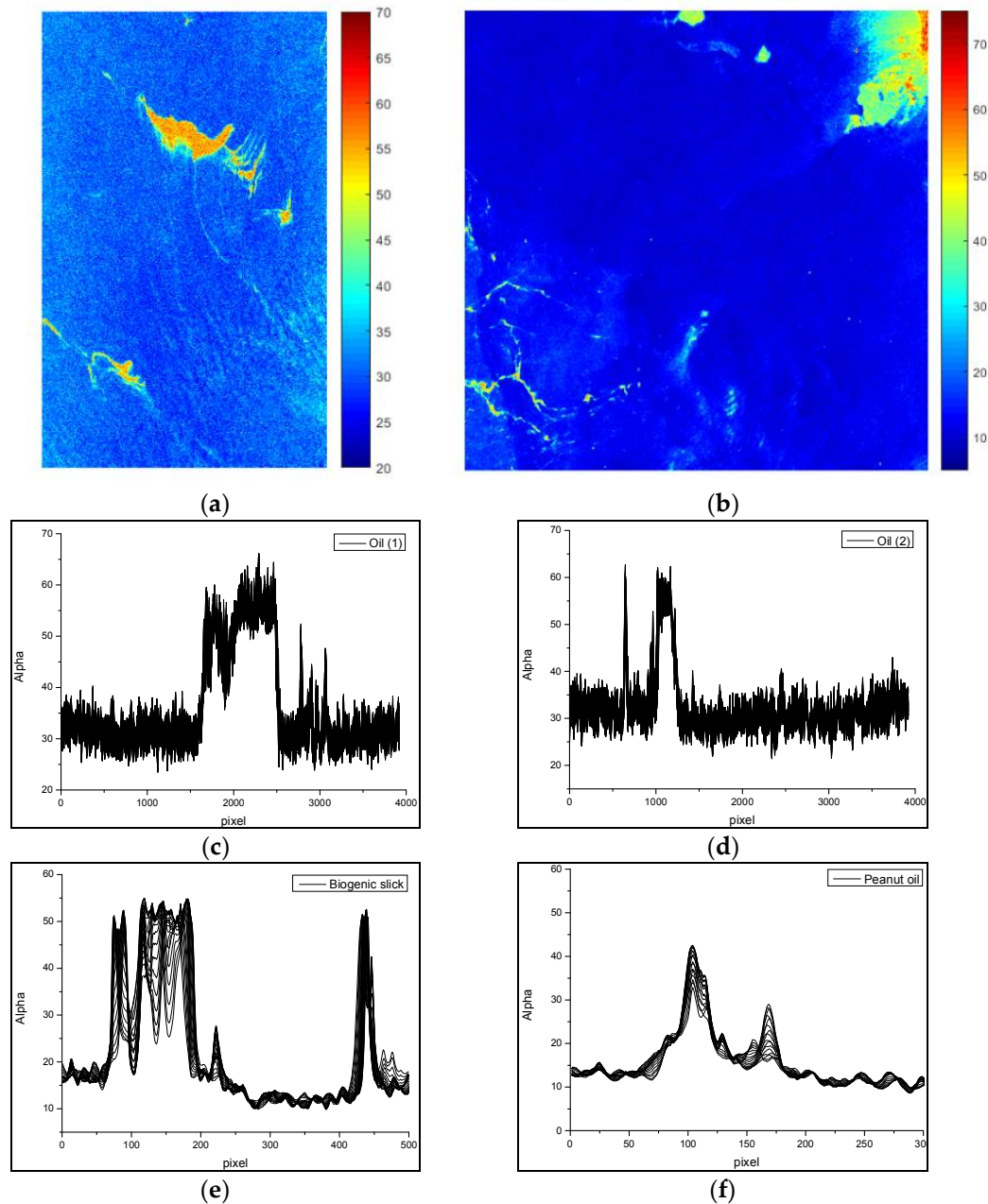


Figure 6. Mean scattering angle (α) for the two continuous slow-release slicks cases mentioned above: (a) Case 1; (b) Case 2; (c–f) the mean scattering angle for the four green rectangular areas (oil (1), oil (2), biogenic slick, and peanut oil, respectively) that are indicated on the SAR images in Figures 2 and 3.

As seen in Figure 7, modified anisotropy A_{12} provides a good visual contrast between slicks and sea in both cases. For Case 1, the oil region, which is primarily dominated by the second eigenvalue λ_2 , has a lower modified anisotropy value when compared to clean seawater. There is a distinct boundary between the thick oil region and the seawater with substantially different values. The range of A_{12} within the thick oil area is approximately 0.1–0.25. In the thin oil region (0.3–0.5), A_{12} has slightly higher values than those in the thick oil region, but still lower than those of ambient sea. A_{12} values

are 0.8–0.95 for the area of clean sea (Figure 7a). It should be noted that the modified anisotropy A_{12} is calculated using the two largest eigenvalues, in case the second and third eigenvalues are seriously affected by noise, which differs from the conventional calculation procedure.

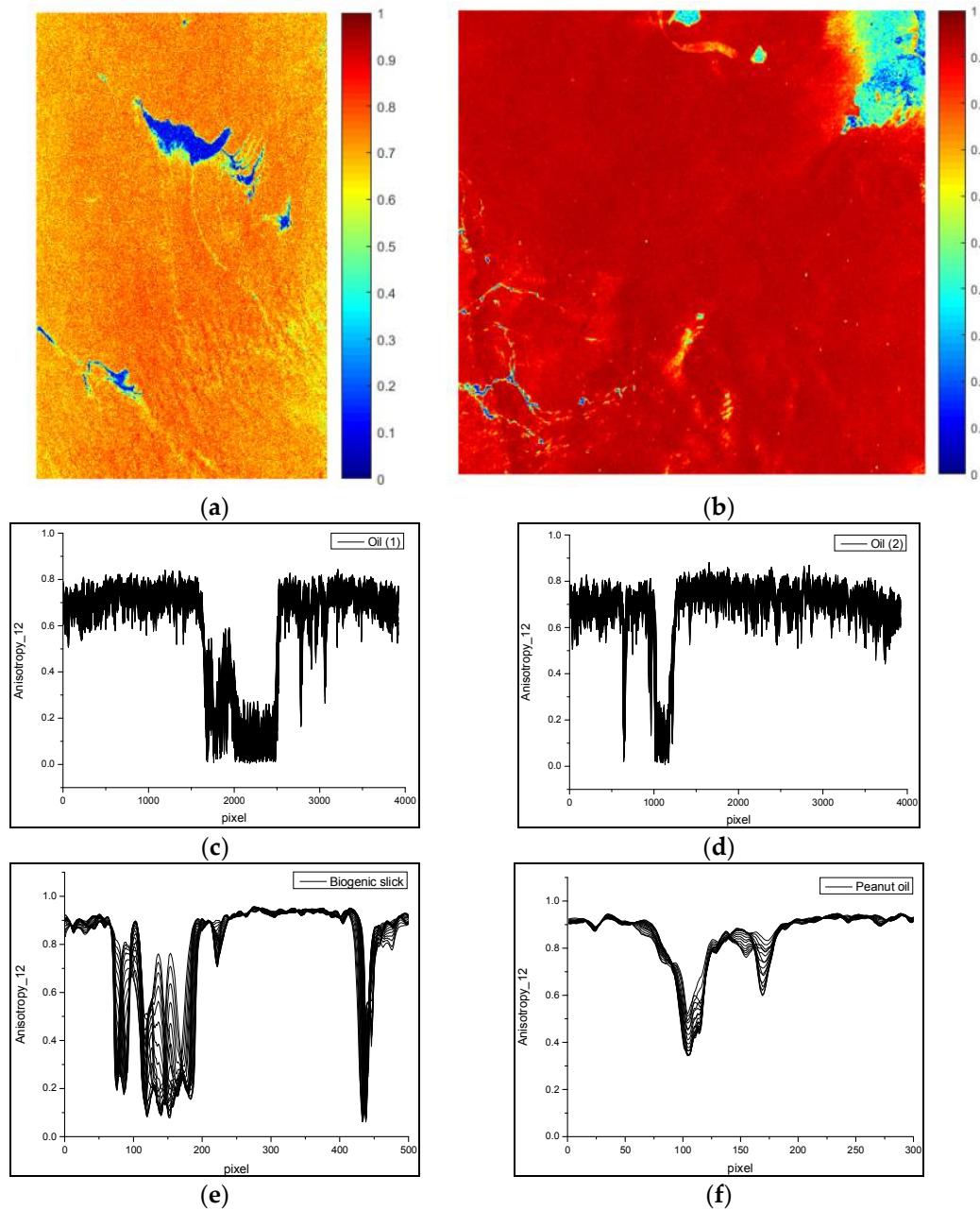


Figure 7. Modified anisotropy (A_{12}) value for the two continuously slow-release slicks cases mentioned above: (a) Case 1; (b) Case 2; (c–f) the modified anisotropy for the four green rectangular areas (oil (1), oil (2), biogenic slick, and peanut oil, respectively) that are indicated on the SAR images in Figures 2 and 3.

Additional results for A_{12} in Case 2 are presented in Figure 7b. A_{12} values in the clean seawater and biogenic slick area show similar trends to those of Case 1. The range of A_{12} values within the biogenic slick region is around 0.2–0.3. The molecular density on the edge of the biogenic slick is relatively low, with sparse monomolecular distribution, and A_{12} range of 0.4–0.6. For the above reasons, the biogenic slicks present as a thinner strip in the image, accompanied by the discontinuous phenomenon.

In addition, the peanut oil poured onto the sea surface is regarded as a type of monomolecular slick to simulate biogenic slick. However, it exhibits much less capacity to suppress sea surface roughness than do biogenic slicks, resulting in A_{12} values within the range of 0.35–0.5.

As shown in Figures 8–10, the combinations of entropy H and modified anisotropy A_{12} , which represent a heuristic modification from the conventional combination of H/A , are used to increase the recognition ability of various scattering types of the target area. The modified combinations are also able to highlight some details concerning changes in the various objectives under different combinations, which have similar purpose and significance to the traditional H/A combinations, i.e., $(1 - H)*(1 - A_{12})$, $(1 - H)*A_{12}$, $H*(1 - A_{12})$, and $H*A_{12}$.

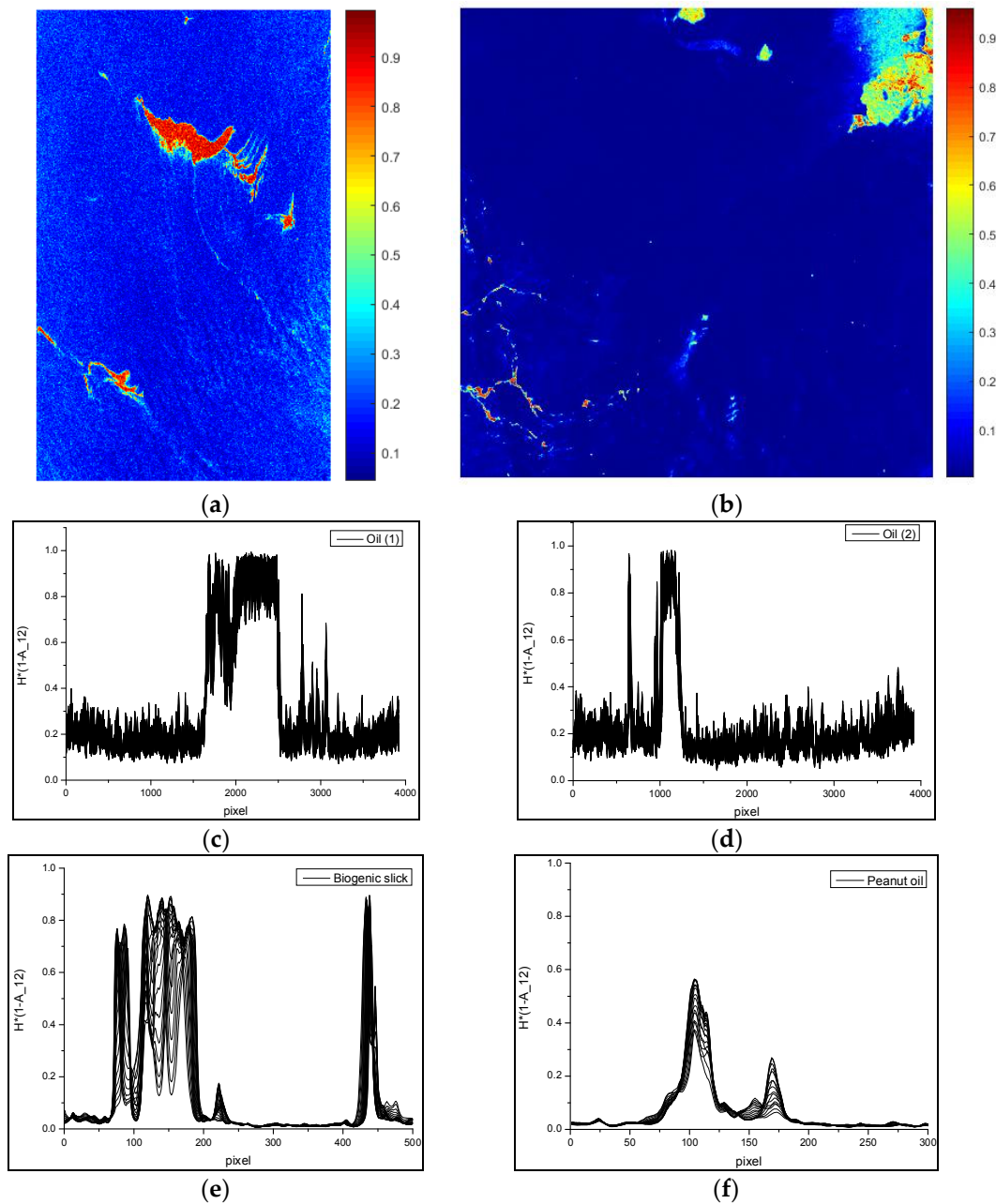


Figure 8. $H*(1 - A_{12})$ value for the two continuously slow-release slicks cases mentioned above: (a) Case 1; (b) Case 2; (c–f) the modified $H*(1 - A_{12})$ for the four green rectangular areas (oil (1), oil (2), biogenic slick, and peanut oil, respectively) that are indicated on the SAR images in Figures 2 and 3.

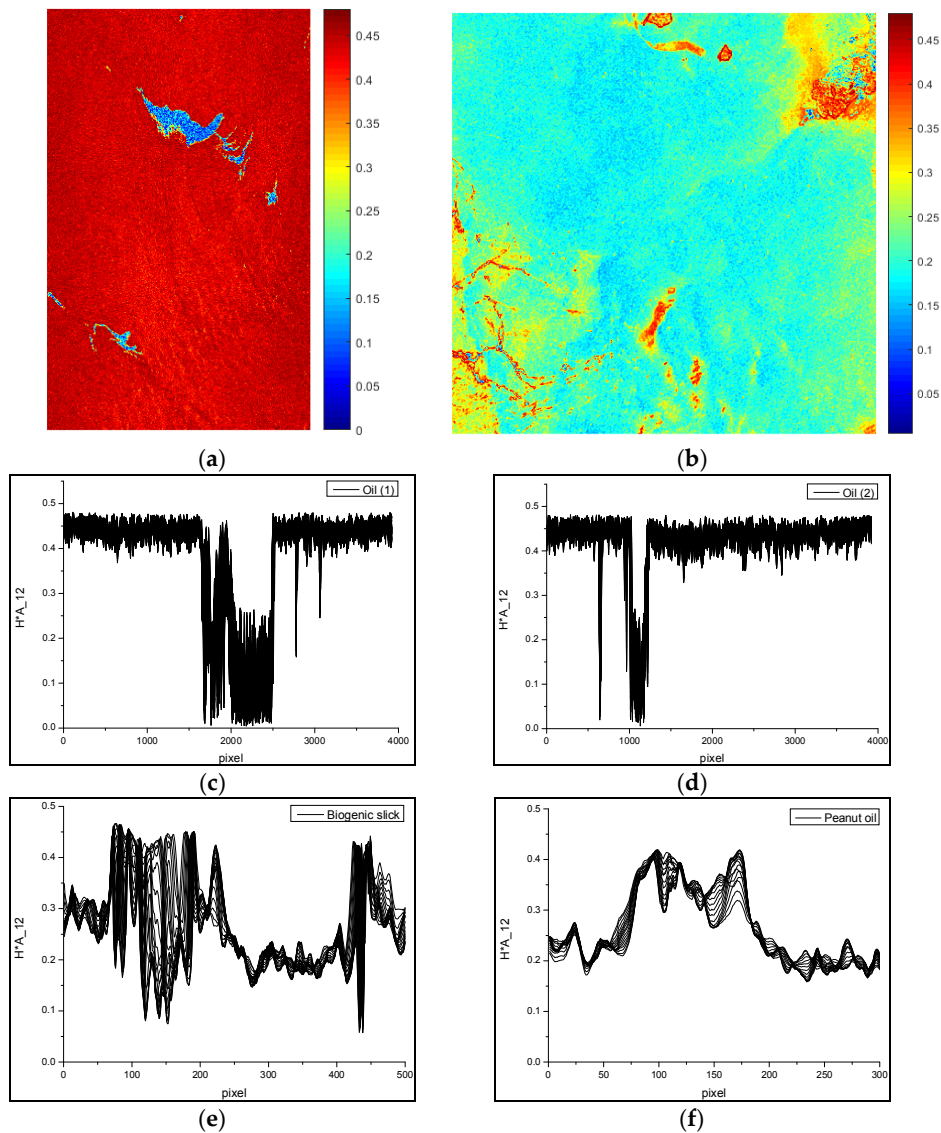


Figure 9. H^*A_{12} value for the two continuously slow-release slicks cases mentioned above: (a) Case 1; (b) Case 2; (c–f) the modified H^*A_{12} for the four green rectangular areas (oil (1), oil (2), biogenic slick, and peanut oil, respectively) that are indicated on the SAR images in Figures 2 and 3.

Figures 8 and 9 show the combined $H^*(1 - A_{12})$ and H^*A_{12} images. In comparison with the traditional H/A combination parameters, the result presents an interesting phenomenon in that the entire $H^*(1 - A_{12})$ image is relatively smooth. This effectively suppresses noise interference, but part of the internal wave region is still misclassified as a thin oil slick, due to similar data characteristics and range in the natural oil seep image. Some interference data remain, similarly to the thin oil slick. In contrast, the thin region at the biogenic slick boundary exhibits similar parameter values to those of peanut oil, but the atmospheric front shows obviously reduced interference in comparison to the peanut oil area; hence, the signal level of the biogenic slick area retains an obvious contrast with the ambient sea. Additional results for H^*A_{12} are presented in Figure 11. In the oil spill image, the modified parameters H^*A_{12} produced a map of the oil spill that effectively suppressed the ambient interference information, i.e., internal waves, which can be used for the extraction and classification of the oil spill. The 3-D spatial distribution plots of $H/\alpha/A_{12}$ and the H/α plane are shown in Figures 10 and 11. These plots can help to better interpret the scattering difference between continuous slow-release slicks and seawater [34].

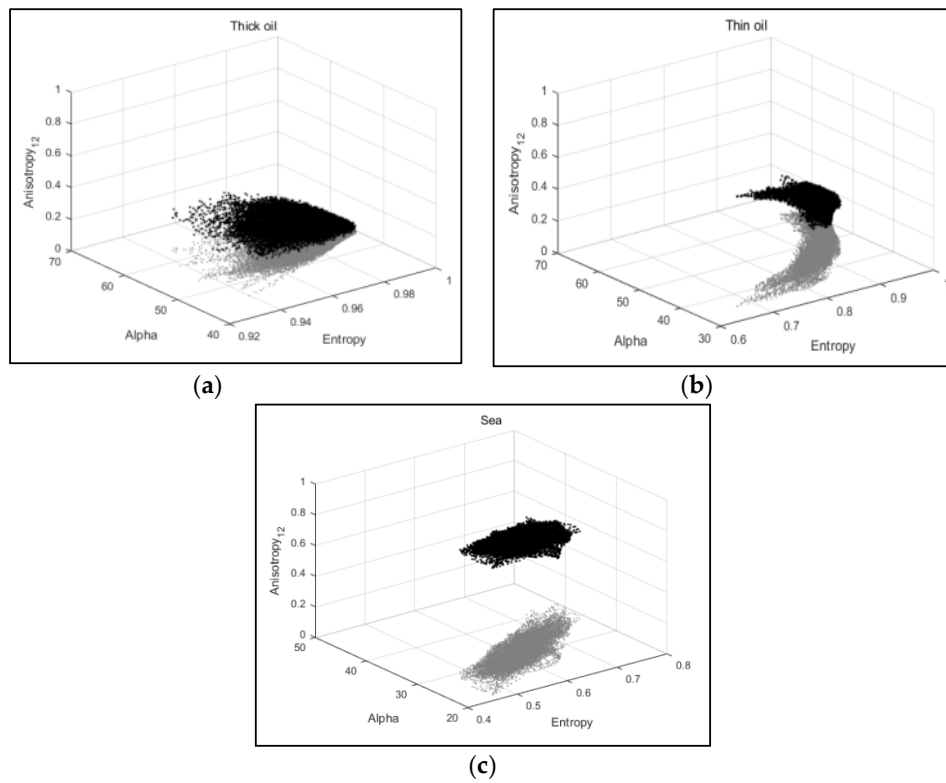


Figure 10. $H/\alpha/A_{12}$ plots for slick and seawater in Case 1. The gray scatter points indicate the H/α plane; (a–c) correspond to the thick oil sample, the thin oil sample, and the clean seawater sample, respectively.

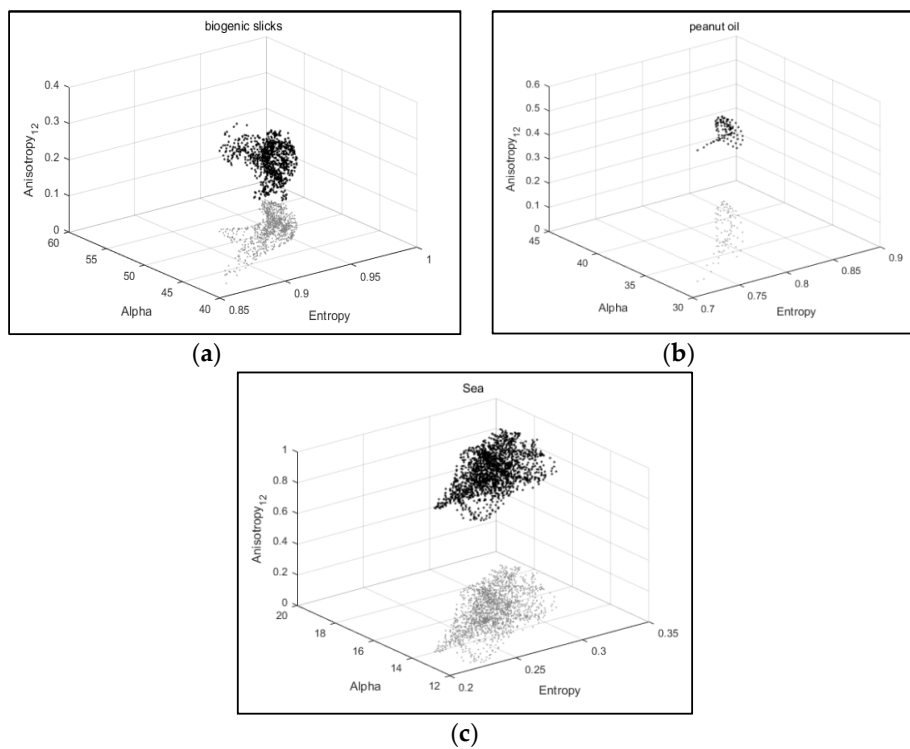


Figure 11. $H/\alpha/A_{12}$ plots for slick and seawater in case (2). The gray scatter points indicate the H/α plane; (a–c) correspond to biogenic slick sample, peanut oil sample and clean seawater sample, respectively.

Figure 12 displays the VSI results. The VSI in the continuously slow-release slick region is obviously higher than that for seawater in both cases, indicating the occurrence of volume scattering within the continuous slow-release slick layer. For Case 1, the image is obviously affected by noise, and the range of VSI values for seawater fluctuate around 0.25–0.45 (average value \sim 0.35). The value within the thick oil slick fluctuates around 0.55, compared with 0.45 within the thin oil slick. Case 2 shows a better SNR, with obviously lower levels of fluctuation of the sample data in the image. The VSI values for biogenic slicks range from 0.4 to 0.5, while those of peanut oil and the atmospheric front areas range from 0.35 to 0.4 and 0.25–0.3, respectively.

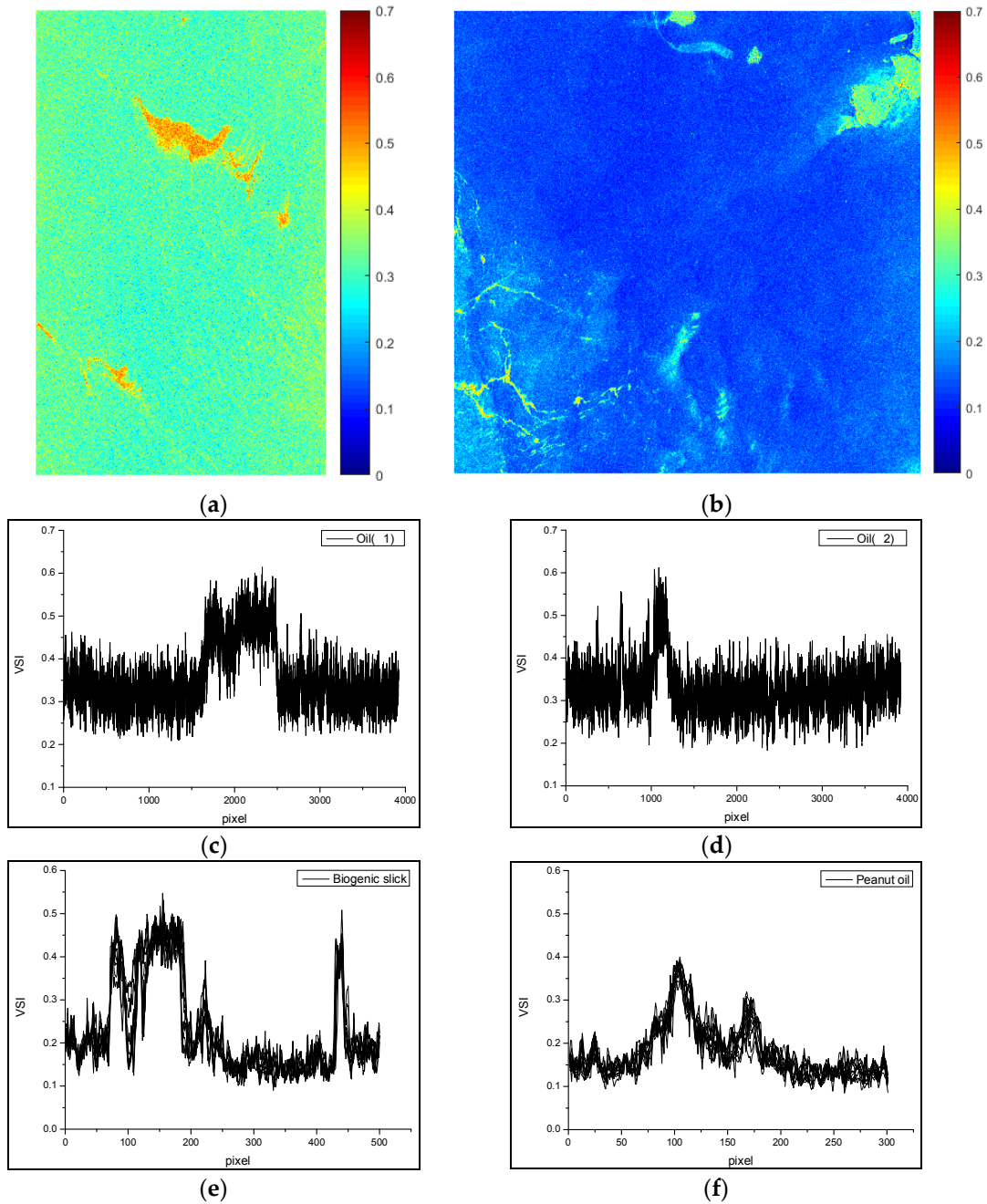


Figure 12. Volume Scattering Index (VSI) values for the two continuously slow-release slicks cases mentioned above: (a) Case 1; (b) Case 2; (c–f) VSI for the four green rectangular areas (oil (1), oil (2), biogenic slick, and peanut oil, respectively) that are indicated on the SAR images in Figures 2 and 3.

4. Discussion

4.1. Analysis of Instrument Noise and NRCS

Surface oil slicks dampen the capillary waves and gravity waves of the sea surface, and reduce small-scale surface roughness and radar backscatter signals. Hence, backscatter from oil slick areas is relatively low when compared to that of the ambient sea, which is more likely to be contaminated by the noise floor. In both the continuous slow-release slick cases, the NRCS of the HH channel is generally lower than that of the VV channel, indicating that the backscatter of the HH channel decreases faster than that of VV. In addition, signals are difficult to distinguish under cross-polarized channels, because the cross-polarized NRCS of both the continuous slow-release slicks are closer to the noise floor and therefore more seriously corrupted by noise. Hence, the VV channel is generally considered more suitable for oil spill detection than HH or the cross-polarized channels. Comparing the image quality and information of the two continuous slow-release oil slick cases, the NESZ baseline of the Case 1 image is higher than that of Case 2; consequently, the signal for the entire SAR image in Case 1 is more seriously contaminated by the noise floor, leading to lower SNR in Case 1. For all the NRCS channels, proximity to the NESZ baseline profoundly affects eigenvalues, eigenvectors, and the associated polarization scattering parameters. Consequently, all parameters of the seawater area in Case 1 are higher than those in Case 2. This phenomenon indicates that, within the same RADARSAT-2 system, a greater proportion of signals in images with large incident angle are contaminated by noise than those with smaller incidence angles of because they are closer to the noise floor. These findings are in accordance with others reported in the literature [18,25].

It should be noted that continuous slow-release slicks are composed of substances released at a fairly slow and relatively constant rate into marine environments, and have a stable slick structure and smooth surface. For Case 1, petroleum is continuously released naturally from the seabed up to the sea surface, such that oil is continually introduced into the bottom layer of the oil slick, accumulating to form an oil layer of a certain thickness. A southeasterly wind prevailed during the period of data collection. On the leeward side, the thin oil at the edge of the slick mixed with seawater. Hence, the NRCS of thick oil is lower than that for thin oil under the co-polarization channel, due to the greater damping effect by of a thick oil layer on the sea surface. For Case 2, biogenic slicks consist of surface-active organic continuously released by marine plants and microorganisms, the data acquisition area is near a popular fishing region off the coast of China's Hainan Island, and the data acquisition period (September) coincides with the greatest biological activity in nearby fisheries. Therefore, a large number of biogenic slicks form dense high concentrations slicks, which appear as smooth, dark stripes. However, the peanut oil that was artificially released onto the sea surface to simulate the biogenic slick in this experiment quickly forms a relatively thin monomolecular slick on the sea surface, due to spontaneous distribution resulting from its molecular characteristics and gravity. The formation process of the two slicks is different. This may explain why the NRCS of the peanut oil is higher than that of biogenic slick.

4.2. Analysis of Polarization Scattering Characteristics

In both of the continuous slow-release slicks, the seawater, which exhibits primarily Bragg scattering that is dominated by the largest eigenvalue λ_1 , has relatively low entropy and high A_{12} . However, as the results (above) show, the seawater in Case 1 exhibits more complex random scattering characteristics than that in Case 2 with the higher H and lower A_{12} , i.e., the surface in Case 1 is more random and is affected by other eigenvalues. There are several possible reasons for this outcome: the incidence angle in Case 1 is 41.9–43.4° (near 45°) and, thus, the signal is contaminated by instrument noise because the NESZ baseline is relatively high; two perpendicular planes on the sea surface form a water dihedral that increases the randomness of the sea surface scattering mechanism when approaching high incidence angle (near 45°), especially at the grazing angle [37].

The continuous slow-release slicks both exhibit complex and highly random scattering characteristics (high entropy and low A_{12}). It is generally believed that the slicks form a certain thickness of surface layer between sea and atmosphere [37,46–48]; thus, the medium consists of three layers—atmosphere, oil slick, and seawater—divided by two special statistically rough interfaces (slick–air interface and slick–water interface) with many possibilities for multiple reflections and scattering in the middle layer. On the other hand, during the formation of continuous slow-release slicks, weathering and emulsification action on the continuous slow-release slick layer may result in oil-in-water emulsification or water -in-oil emulsification. Hence, the randomness of the volume scattering component may be increased in the slick layer.

For Case 2, the biogenic slick and peanut oil (surfactant) are often used as the same type of monomolecular slicks for comparison and study [13,30,35,36]. As the results (above) show, the continuous slow-release (biogenic) slick exhibits greater damping and more complex random scattering characteristics than anthropogenic ocean surface slicks (peanut oil), this could be explained by the difference in the formation process of the slicks. It should be noted that peanut oil released on the sea surface forms monomolecular slicks because of its special amphiphilic structure, which can be used to simulate biogenic slicks. Thus, in this study, the scattering results of the effective peanut oil area produced by five liters of peanut oil are considered to be an acceptable reference for future research on the influence and mechanisms of marine slick formation processes.

5. Conclusions

Quad-polarization SAR provides an effective tool for detecting oil spills, and has the capacity to provide comprehensive and abundant polarization information about marine oil slicks. In this study, the polarization scattering characteristics of two typical continuous slow-release slicks were investigated under the quad-polarization RADARSAT-2 system. The signal levels of the samples and instruments were examined at different incident angles to explore the influence of SNR on subsequent analysis and results. Furthermore, possible scattering mechanisms of continuous slow-release slicks, anthropogenic ocean surface slicks, and seawater are explored and analyzed based on the modified polarization decomposition parameter combination $H/\alpha/A_{12}$ and VSI. It needs to be emphasized that the continuous slow-release slicks in different sea areas and origins will have different characteristics and size information. The more abundant and comprehensive study is necessary to explore the continuous slow-release slicks in the future. The main findings of this study are as follows:

- Images acquired at small incident angles have higher SNR than those with large incident angles under the same RADARSAT-2 system. The NRCS of cross-polarization channels are lower than those of co-polarization channels, which are more seriously affected by the noise floor because of their proximity to the NESZ baseline.
- The polarimetric scattering properties of continuous slow-release slicks differ from those of clean seawater, even for anthropogenic ocean surface slicks, since continuous slow-release slicks exhibit complex, multiple scattering mechanisms, possibly as a result of the comprehensive influence of surface scattering, volume scattering, and the noise floor. In addition, continuous slow-release (biogenic) slicks exhibit greater damping characteristics and more complex random scattering characteristics than anthropogenic ocean surface slicks (simulated with peanut oil) in this experiment.
- For slick detection, the combinations of entropy (H) and modified anisotropy (A_{12}) permit fairly robust identification of slicks from SAR images under different sea conditions.

Previous studies have concluded that there are many factors that affect the polarimetric scattering characteristics of oil spills, including environmental factors (e.g., wind speed, waves, sea currents, sea temperature, seawater composition, climate, and light intensity), instrument design parameters (polarization, incident angle, bandwidth, noise floor, instrument precision), and oil slick information

(oil type, age, thickness, formation process, and reason for formation). More detailed research on continuous slow-release marine oil slicks is planned.

Author Contributions: G.L. conceived and performed the experiments; Y.L. and B.L. supervised and designed the research and contributed to the article's organization; Y.H. and J.F. carried out the comparative analysis. G.L. drafted the manuscript, which was revised by all authors. All authors read and approved the final manuscript.

Funding: This article was supported by Fundamental Research Funds for the Central Universities (Grant No. 3132014302), the National Natural Science Foundation of China (Grant Nos. 51509030 and 41571336) and National Marine Public Welfare Project (Grant No. 201305002).

Acknowledgments: We thank Ridha Touzi and Stefan Nedelcu from the Canada Centre for Remote Sensing for advice regarding polarimetry and data-processing software. We also acknowledge Fengshou Zhang and Shiyong Wen of the National Marine Environmental Monitoring Center for processing the data.

Conflicts of Interest: The authors declare no conflict of interest.

References

1. Fingas, M.; Brown, C. A review of oil spill remote sensing. *Sensors (Basel)* **2018**, *2*, 91.
2. Hou, Y.; Li, Y.; Liu, B.; Liu, Y.; Wang, T. Design and implementation of a coastal-mounted sensor for oil film detection on seawater. *Sensors (Basel)* **2018**, *2*, 70. [[CrossRef](#)] [[PubMed](#)]
3. Liu, B.; Li, Y.; Liu, C.; Xie, F.; Muller, J.-P. Hyperspectral features of oil-polluted sea ice and the response to the contamination area fraction. *Sensors (Basel)* **2018**, *2*, 234. [[CrossRef](#)] [[PubMed](#)]
4. Cui, C.; Li, Y.; Liu, B.; Li, G. A new endmember preprocessing method for the hyperspectral unmixing of imagery containing marine oil spills. *ISPRS Int. J. Geo-Inf.* **2017**, *9*, 286. [[CrossRef](#)]
5. Alves, T.M.; Kokinou, E.; Zodiatis, G.; Lardner, R. Hindcast, GIS and susceptibility modelling to assist oil spill clean-up and mitigation on the southern coast of Cyprus (Eastern Mediterranean). *Deep Sea Res. Part II Top. Stud. Oceanogr.* **2016**, *133*, 159–175. [[CrossRef](#)]
6. Alves, T.M.; Kokinou, E.; Zodiatis, G. A three-step model to assess shoreline and offshore susceptibility to oil spills: The South Aegean (Crete) as an analogue for confined marine basins. *Mar. Pollut. Bull.* **2014**, *86*, 443–457. [[CrossRef](#)] [[PubMed](#)]
7. Alves, T.M.; Kokinou, E.; Zodiatis, G. Modelling of oil spills in confined maritime basins: The case for early response in the Eastern Mediterranean Sea. *Environ. Pollut.* **2015**, *206*, 390–399. [[CrossRef](#)] [[PubMed](#)]
8. Alves, T.M.; Kokinou, E.; Zodiatis, G. Multidisciplinary oil spill modeling to protect coastal communities and the environment of the Eastern Mediterranean Sea. *Sci. Rep.* **2016**, *6*, 36882. [[CrossRef](#)] [[PubMed](#)]
9. Kvenvolden, K.A.; Cooper, C.K. Natural seepage of crude oil into the marine environment. *Geo-Mar. Lett.* **2003**, *3–4*, 140–146. [[CrossRef](#)]
10. Transportation Research Board and National Research Council. *Oil in the Sea III: Inputs, Fates, and Effects*; National Academies Press: Washington, DC, USA, 2003.
11. DiGiacomo, P.M.; Washburn, L.; Holt, B. Coastal pollution hazards in southern California observed by SAR imagery: Stormwater plumes, wastewater plumes, and natural hydrocarbon seeps. *Mar. Pollut. Bull.* **2004**, *11–12*, 1013–1024. [[CrossRef](#)] [[PubMed](#)]
12. Hu, C.; Li, X.; Pichel, W.G.; Muller-Karger, F.E. Detection of natural oil slicks in the NW Gulf of Mexico using MODIS imagery. *Geophys. Res. Lett.* **2009**, *1*, L01604. [[CrossRef](#)]
13. Hühnerfuss, H. Basic physicochemical principles of monomolecular sea slicks and crude oil spills. In *Marine Surface Films*; Gade, M., Hühnerfuss, H., Korenowski, G.M., Eds.; Springer: Berlin/Heidelberg, Germany, 2006; pp. 21–35.
14. de Araújo Carvalho, G.; Minnett, P.J.; de Miranda, F.P.; Landau, L.; Paes, E.T. Exploratory data analysis of synthetic aperture radar (SAR) measurements to distinguish the sea surface expressions of naturally-occurring oil seeps from human-related oil spills in Campeche Bay (Gulf of Mexico). *ISPRS Int. J. Geo-Inf.* **2017**, *12*, 379. [[CrossRef](#)]
15. Fingas, M.; Brown, C. Review of oil spill remote sensing. *Mar. Pollut. Bull.* **2014**, *1*, 9–23. [[CrossRef](#)] [[PubMed](#)]
16. Garcia-Pineda, O.; Holmes, J.; Rissing, M.; Jones, R.; Wobus, C.; Svejkovsky, J.; Hess, M. Detection of oil near shorelines during the Deepwater Horizon oil spill using synthetic aperture radar (SAR). *Remote Sens.* **2017**, *6*, 567. [[CrossRef](#)]

17. Hu, J.; Ghamisi, P.; Schmitt, A.; Zhu, X.-X. Object based fusion of polarimetric SAR and hyperspectral imaging for land use classification. In Proceedings of the 8th Workshop on Hyperspectral Image and Signal Processing: Evolution in Remote Sensing (WHISPERS), Los Angeles, CA, USA, 21–24 August 2016; pp. 1–5.
18. Minchew, B.; Jones, C.E.; Holt, B. Polarimetric analysis of backscatter from the Deepwater Horizon oil spill using L-Band synthetic aperture radar. *IEEE Trans. Geosci. Remote Sens.* **2012**, *10*, 3812–3830. [[CrossRef](#)]
19. Zhang, B.; Perrie, W.; Li, W.; Pichel, W.G. Mapping sea surface oil slicks using RADARSAT-2 quad-polarization SAR image. *Geophys. Res. Lett.* **2011**, *38*. [[CrossRef](#)]
20. Alpers, W.; Hühnerfuss, H. Radar signatures of oil films floating on the sea surface and the Marangoni effect. *J. Geophys. Res. Oceans* **1988**, *C4*, 3642–3648. [[CrossRef](#)]
21. Holt, B. SAR imaging of the ocean surface. In *Synthetic Aperture Radar Marine User's Manual*; Jackson, C.R., Apel, J.R., Eds.; Available online: <http://www.sarusersmanual.com/> (accessed on 10 June 2018).
22. Reddy, C.M. While oil gently seeps from the seafloor: Oil naturally leaking into the ocean offers a 'laboratory' to study accidental spills. *Oceanus* **2009**, *3*, 231–244.
23. Delpeche-Ellmann, N.C.; Soomere, T. Investigating the Marine Protected Areas most at risk of current-driven pollution in the Gulf of Finland, the Baltic Sea, using a Lagrangian transport model. *Mar. Pollut. Bull.* **2013**, *1–2*, 121–129. [[CrossRef](#)] [[PubMed](#)]
24. Lardner, R.; Zodiatis, G. Modelling oil plumes from subsurface spills. *Mar. Pollut. Bull.* **2017**, *1*, 94–101. [[CrossRef](#)] [[PubMed](#)]
25. Skrunes, S.; Brekke, C.; Eltoft, T. Characterization of marine surface slicks by Radarsat-2 multipolarization features. *IEEE Trans. Geosci. Remote Sens.* **2014**, *9*, 5302–5319. [[CrossRef](#)]
26. Nunziata, F.; Gambardella, A.; Migliaccio, M. On the degree of polarization for SAR sea oil slick observation. *ISPRS J. Photogramm. Remote Sens.* **2013**, *4*, 41–49. [[CrossRef](#)]
27. Salberg, A.-B.; Rudjord, O.; Schistad Solberg, A.H. Oil spill detection in hybrid-polarimetric SAR images. *IEEE Trans. Geosci. Remote Sens.* **2014**, *10*, 6521–6533. [[CrossRef](#)]
28. Li, Y.; Zhang, Y.; Chen, J.; Zhang, H. Improved compact polarimetric SAR quad-pol reconstruction algorithm for oil spill detection. *IEEE Geosci. Remote Sens. Lett.* **2014**, *11*, 1139–1142. [[CrossRef](#)]
29. Zatyagalova, V.V.; Ivanov, A.Y.; Golubov, B.N. Application of Envisat SAR imagery for mapping and estimation of natural oil seeps in the South Caspian Sea, 2007. In Proceedings of the 'Envisat Symposium 2007', Montreux, Switzerland, 23–27 April 2007.
30. Guo, H.; Wu, D.; An, J. Discrimination of oil slicks and lookalikes in polarimetric SAR images using CNN. *Sensors (Basel)* **2017**, *8*, 1837. [[CrossRef](#)] [[PubMed](#)]
31. Li, X.; Li, C.; Yang, Z.; Pichel, W. SAR imaging of ocean surface oil seep trajectories induced by near inertial oscillation. *Remote Sens. Environ.* **2013**, *130*, 182–187. [[CrossRef](#)]
32. De Maio, A.; Orlando, D.; Pallotta, L.; Clemente, C. A Multifamily GLRT for Oil Spill Detection. *IEEE Trans. Geosci. Remote Sens.* **2017**, *55*, 63–79. [[CrossRef](#)]
33. Pallotta, L.; Clemente, C.; De Maio, A.; Soraghan, J.J. Detecting Covariance Symmetries in Polarimetric SAR Images. *IEEE Trans. Geosci. Remote Sens.* **2017**, *55*, 80–95. [[CrossRef](#)]
34. Migliaccio, M.; Gambardella, A.; Tranfaglia, M. SAR polarimetry to observe oil spills. *IEEE Trans. Geosci. Remote Sens.* **2007**, *45*, 506–511. [[CrossRef](#)]
35. Tian, W.; Shao, Y.; Yuan, J.; Wang, S.; Liu, Y. An experiment for oil spill recognition using RADARSAT-2 image. In Proceedings of the 2010 IEEE International Geoscience and Remote Sensing Symposium (IGARSS), Honolulu, HI, USA, 25–30 July 2010; pp. 2761–2764.
36. Gade, M.; Alpers, W.; Hühnerfuss, H.; Masuko, H.; Kobayashi, T. Imaging of biogenic and anthropogenic ocean surface films by the multifrequency/multipolarization SIR-C/X-SAR. *J. Geophys. Res. Oceans* **1998**, *103*, 18851–18866. [[CrossRef](#)]
37. Li, H.; Perrie, W.; He, Y.; Wu, J.; Luo, X. Analysis of the polarimetric SAR scattering properties of oil-covered waters. *IEEE J.-Stars* **2015**, *8*, 3751–3759. [[CrossRef](#)]
38. Schuler, D.L.; Lee, J.S. Mapping ocean surface features using biogenic slick-fields and SAR polarimetric decomposition techniques. *IEEE Proc. Radar Sonar Navig.* **2006**, *3*, 260–270. [[CrossRef](#)]
39. Garcia-Pineda, O.; Zimmer, B.; Howard, M.; Pichel, W.; Li, X.; MacDonald, I.R. Using SAR images to delineate ocean oil slicks with a texture-classifying neural network algorithm (TCNNA). *Can. J. Remote Sens.* **2009**, *5*, 411–421. [[CrossRef](#)]

40. Jones, C.E.; Minchew, B.; Holt, B.; Hensley, S. Studies of the Deepwater Horizon oil spill with the UAVSAR radar. In *Monitoring and Modeling the Deepwater Horizon Oil Spill: A Record-Breaking Enterprise, 1*; Liu, Y., MacFadyen, A., Ji, Z.-G., Weisberg, R.H., Eds.; American Geophysical Union: Washington, DC, USA, 2013.
41. Cloude, S.R.; Pottier, E. An entropy based classification scheme for land applications of polarimetric SAR. *IEEE Trans. Geosci. Remote Sens.* **1997**, *1*, 68–78. [[CrossRef](#)]
42. Haldar, D.; Patnaik, C.; Mohan, S. Jute and tea discrimination through fusion of SAR and optical data. *Prog. Electromagn. Res. B* **2012**, *39*, 337–354. [[CrossRef](#)]
43. Pope, K.O.; Rey-Benayas, J.M.; Paris, J.F. Radar remote sensing of forest and wetland ecosystems in the Central American tropics. *Remote Sens. Environ.* **1994**, *2*, 205–219. [[CrossRef](#)]
44. Cloude, S.R.; Pottier, E. A review of target decomposition theorems in radar polarimetry. *IEEE Trans. Geosci. Remote Sens.* **1996**, *2*, 498–518. [[CrossRef](#)]
45. Lee, J.-S.; Pottier, E. *Polarimetric Radar Imaging: From Basics to Applications*; CRC Press: Boca Raton, FL, USA, 2009.
46. Plant, W.J.; Keller, W.C.; Hayes, K.; Chatham, G. Normalized radar cross section of the sea for backscatter: 1. Mean levels. *J. Geophys. Res.* **2010**, *C9*. [[CrossRef](#)]
47. Raney, R.K.; Cahill, J.T.S.; Patterson, G.W.; Bussey, D.B.J. The m-chi decomposition of hybrid dual-polarimetric radar data with application to lunar craters. *J. Geophys. Res. Planets* **2012**, *E12*. [[CrossRef](#)]
48. Hapke, B.W.; Nelson, R.M.; Smythe, W.D. The opposition effect of the moon: The contribution of coherent backscatter. *Science* **1993**, *5107*, 509–511. [[CrossRef](#)] [[PubMed](#)]



© 2018 by the authors. Licensee MDPI, Basel, Switzerland. This article is an open access article distributed under the terms and conditions of the Creative Commons Attribution (CC BY) license (<http://creativecommons.org/licenses/by/4.0/>).